

Chemical Erosion of Carbon–Carbon/Graphite Nozzles in Solid-Propellant Rocket Motors

Piyush Thakre* and Vigor Yang†

Pennsylvania State University, University Park, Pennsylvania 16802

DOI: 10.2514/1.34946

A comprehensive theoretical/numerical framework is established and validated to study the chemical erosion of carbon–carbon/graphite nozzle materials in solid-rocket motors at practical operating conditions. The formulation takes into account detailed thermofluid dynamics for a multicomponent reacting flow, heterogeneous reactions at the nozzle surface, condensed-phase energy transport, and nozzle material properties. Many restrictive assumptions and approximations made in the previous models have been relaxed. Both metallized and nonmetallized AP/HTPB composite propellants are treated. The predicted nozzle surface recession rates compare well with three different sets of experimental data. The erosion rate follows the trend exhibited by the heat-flux distribution and is most severe in the throat region. H₂O proved to be the most detrimental oxidizing species in dictating nozzle erosion, followed by much lesser contributions from OH and CO₂, in that order. The erosion rate increases with increasing chamber pressure, mainly due to higher convective heat transfer and enhanced heterogeneous surface reactions. For nonmetallized propellants, the recession rate is dictated by heterogeneous chemical kinetics because the nozzle surface temperature is relatively low. For metallized propellants, the process is diffusion-controlled due to the high surface temperature. The erosion rate decreases with increasing aluminum content, a phenomenon resulting from reduced concentrations of oxidizing species H₂O, OH, and CO₂. The transition from the kinetics-controlled to diffusion-controlled mechanism occurs at a surface temperature of around 2800 K.

Nomenclature

A_i	= preexponential factor for rate constant in reaction i
b_i	= temperature exponent for rate constant in reaction i
C_p	= constant-pressure specific heat
Da	= Damköhler number
D_{ij}	= binary mass diffusivity
D_{im}	= molecular mass diffusivity
E	= specific total internal energy
E_i	= activation energy for reaction i
h	= enthalpy
k	= turbulent kinetic energy
Le	= Lewis number
Le_t	= turbulent Lewis number
\dot{m}	= mass flow rate
N	= total species numbers
Pr	= Prandtl number
Pr_t	= turbulent Prandtl number
p	= pressure
p_t	= chamber pressure
R	= particular gas constant
Re	= Reynolds number
R_u	= universal gas constant
\dot{r}_c	= net surface recession rate, m/s
$\dot{r}_{i,erosion}$	= recession rate due to species i , kg/m ² -s
$\dot{r}_{i,ch}$	= chemical-kinetics-controlled recession rate due to species i , kg/m ² -s
$\dot{r}_{i,diff-lim}$	= diffusion-controlled recession rate due to species i , kg/m ² -s
Sc	= Schmidt number

Sc_t	= turbulent Schmidt number
T	= temperature
T_t	= chamber temperature
U_k	= mass diffusion velocity of species k
u, v, w	= x, y, z component of velocity respectively
W_k	= molecular weight of species k
W_{mix}	= average molecular weight of the gases
\dot{w}	= species molar production rate
X_k	= mole fraction of species k
Y_k	= mass fraction of species k
α	= thermal diffusivity
γ	= ratio of specific heats
ε	= dissipation rate
κ	= von Kármán constant
λ	= thermal conductivity
μ	= viscosity
μ_t	= turbulent viscosity
ρ	= density
$\dot{\omega}$	= species mass production rate
$\omega_{i,diff-lim}$	= maximum diffusion rate of species i toward the surface, kg/m ² -s
$-$	= time average
\sim	= mass-weighted average (Favre average)

Subscripts

amb	= ambient conditions
c	= solid phase
g	= gas phase
$c-g$	= gas–solid interface
o	= outer boundary of nozzle material
s	= surface

Superscript

+	= nondimensional variable
---	---------------------------

I. Introduction

GRAPHITE and carbon–carbon composites, which have excellent thermophysical properties as well as low densities, are widely used as materials for rocket-nozzle inserts. The hostile thermochemical environment imposed by the combustion products

Presented as Paper 5777 at the 43rd AIAA/ASME/SAE/ASEE Joint Propulsion Conference, Cincinnati, OH, 8–11 July 2007; received 2 October 2007; revision received 10 April 2008; accepted for publication 11 April 2008. Copyright © 2008 by Authors. Published by the American Institute of Aeronautics and Astronautics, Inc., with permission. Copies of this paper may be made for personal or internal use, on condition that the copier pay the \$10.00 per-copy fee to the Copyright Clearance Center, Inc., 222 Rosewood Drive, Danvers, MA 01923; include the code 0748-4658/08 \$10.00 in correspondence with the CCC.

*Ph.D. Candidate, Department of Mechanical and Nuclear Engineering; ptk109@psu.edu. Member AIAA.

†John L. and Genevieve H. McCain Chair in Engineering, Department of Mechanical and Nuclear Engineering; vigor@psu.edu. Fellow AIAA.

of solid propellants, however, causes undesirable erosion of these materials. During motor operation, the temperature of the nozzle material rises rapidly, due to the severe heat transfer from the hot combustion products to the nozzle surface. Heterogeneous chemical reactions occur between the nozzle material and such oxidizing species as H_2O , OH , and CO_2 in the combustion stream. The ensuing chemical erosion then causes the nozzle surface to recede. The situation becomes most severe at the throat, due to the maximized heat-transfer rate in that region. The resultant increase in the throat area decreases the chamber pressure and thrust and subsequently downgrades the motor performance over the duration of firing. A throat-area increase of more than 5% is usually considered unacceptable for most solid-rocket applications [1].

The overall nozzle-erosion process is extremely complex, comprising the interplay of numerous factors, including the propellant composition, motor operating conditions, duration of firing, nozzle geometry and material properties, transport of reacting species, and homogeneous and heterogeneous reactions in the gas phase and at the nozzle surface, respectively. In addition to chemical erosion, there could be contributions from mechanical processes associated with the impingement of metal oxide particles (e.g., $Al_2O_{3(l)}$) onto the nozzle surface and from the thermal-stress-induced structural failure. Most studies [2–6], however, have concluded that chemical erosion is the primary cause for the nozzle-throat recession. Moreover, mechanical erosion caused by the impingement of Al_2O_3 particles is negligible in the throat region because the particles travel almost parallel to the surface [1]. Experimental studies [2,6,7] on graphite nozzle erosion with aluminized composite solid propellants have indicated that the graphite removal depended primarily on the chemical attack by the oxidizing species of H_2O and CO_2 . A strong correlation was noted between the recession rate at the throat and the mass fractions of H_2O and CO_2 . The nozzle erosion decreased with increasing aluminum content in the propellant [2]. The phenomenon can be attributed to the decreased concentrations of H_2O and CO_2 in the combustion stream. If mechanical processes were significant, then the throat erosion would have increased with the increase of condensed-phase Al_2O_3 particles in the combustion stream, but, on the contrary, the erosion decreased.

In the 1960s and 1970s, with limited computational resources and a lack of in-depth knowledge, many investigators [3–5,8] developed simplistic models to predict the nozzle-throat recession rate. It was pointed out [3,4] that the erosion rate depends on the heterogeneous chemical kinetics at the surface as well as the diffusion of the oxidizing species toward the surface. A more detailed model was later developed by Kuo and Keswani [9] and Keswani and Kuo [10]. This work represents a significant improvement over the earlier approaches and predicts the nozzle-throat recession rates reasonably well. Some of the underlying assumptions and approximations, however, may not be necessary or justified in many situations. One of the major assumptions includes empirically calculating the recession rate as the harmonic mean of the kinetics- and diffusion-limited rates. This approach is valid only if the heterogeneous reactions are first order, the effective Schmidt numbers for all reactants are nearly equal, and the surface mass blowing is not too strong [10]. The assumption of first-order reactions strongly restricts the kind of surface kinetics that can be adopted. Moreover, the harmonic-mean approximation becomes questionable in situations in which the kinetics- and diffusion-limited rates are on the same order of magnitude. The model employs the boundary-layer approximation for solving the gas-phase conservation equations and neglects the effect of surface-reaction products on the nozzle erosion in the downstream region. Other approximations include the unity Lewis number, a single binary diffusion coefficient applied to all the species, a constant Prandtl number, and the use of infinitely fast heterogeneous kinetics (infinite Damköhler number) in obtaining the solution to the gas-phase species equations. Another nozzle-erosion model subsequently developed by Borie et al. [11] bears a close resemblance to that of Kuo and Keswani [9]. More recently, Acharya and Kuo [12] updated the model of Kuo and Keswani [9] by adopting improved heterogeneous kinetics at the nozzle surface. The underlying assumptions and approximations, however, remain identical to their previous model.

The purpose of the current work is to present a comprehensive theoretical/numerical framework that can accurately predict the nozzle-erosion rate by using recent advances in chemical kinetics, turbulence modeling, and numerical algorithm. Many approximations and assumptions employed in the previous studies have been relaxed. The formulation takes into account detailed thermofluid dynamics for a multicomponent chemically reacting flow, heterogeneous reactions at the nozzle surface, and condensed-phase energy transport. The model was validated by comparing the calculated erosion rates with three different sets of experimental data. In addition, a systematic study of the dependence of nozzle erosion on motor operating conditions, chemical kinetics, propellant compositions, and nozzle material properties was carried out.

II. Theoretical Formulation

The theoretical formulation involves the general conservation laws for the gas phase, the energy equation for the solid phase, and the boundary conditions at the gas–solid interface and the outer surface of the nozzle material.

A. Gas-Phase Governing Equations

The gas-phase dynamics are modeled using the Favre-averaged conservation equations of mass, momentum, energy, and species concentration in axisymmetric coordinates.

Mass:

$$\frac{\partial \bar{\rho}}{\partial t} + \frac{\partial \bar{\rho} \tilde{u}_i}{\partial x_i} = 0 \quad (1)$$

Momentum:

$$\frac{\partial \bar{\rho} \tilde{u}_i}{\partial t} + \frac{\partial (\bar{\rho} \tilde{u}_i \tilde{u}_j)}{\partial x_j} = -\frac{\partial \bar{p}}{\partial x_i} + \frac{\partial (\bar{\tau}_{ij} - \overline{\rho u_i'' u_j''})}{\partial x_j} \quad (2)$$

Energy:

$$\frac{\partial \bar{\rho} \tilde{E}}{\partial t} + \frac{\partial [(\bar{\rho} \tilde{E} + \bar{p}) \tilde{u}_i]}{\partial x_i} = -\frac{\partial \bar{q}_i}{\partial x_i} + \frac{\partial (\bar{u}_i \bar{\tau}_{ij} - \overline{\rho E'' u_j''})}{\partial x_j} \quad (3)$$

Species concentration:

$$\frac{\partial \bar{\rho} \tilde{Y}_k}{\partial t} + \frac{\partial (\bar{\rho} \tilde{Y}_k \tilde{u}_j)}{\partial x_j} = \bar{\omega}_k + \frac{\partial (-\bar{\rho} \tilde{Y}_k \tilde{U}_{k,j} - \overline{\rho Y_k'' u_j''})}{\partial x_j} \quad k = 1, \dots, N \quad (4)$$

The viscous stress tensor τ_{ij} and the heat-flux vector q_i are expressed, respectively, as

$$\bar{\tau}_{ij} = \mu \left(\frac{\partial \tilde{u}_i}{\partial x_j} + \frac{\partial \tilde{u}_j}{\partial x_i} - \frac{2}{3} \delta_{ij} \frac{\partial \tilde{u}_l}{\partial x_l} \right) \quad (5)$$

$$\bar{q}_i = -\lambda \frac{\partial \tilde{T}}{\partial x_i} + \bar{\rho} \sum_{k=1}^N \tilde{h}_k \tilde{Y}_k \tilde{U}_{k,i} \quad (6)$$

Fick's law is used to approximate the species diffusion in a multicomponent mixture:

$$\tilde{Y}_k \tilde{U}_{k,i} = -D_{km} \frac{\partial \tilde{Y}_k}{\partial x_i} \quad (7)$$

The specific total internal energy, specific enthalpy, and pressure for a multicomponent mixture can be calculated from the following equations:

$$\tilde{E} = \tilde{h} - \frac{\bar{p}}{\bar{\rho}} + \frac{\tilde{u}_j \tilde{u}_j}{2} \quad (8)$$

$$\tilde{h} = \sum_{k=1}^N \tilde{Y}_k \tilde{h}_k = \sum_{k=1}^N \tilde{Y}_k \left(\Delta h_{f,k}^\circ + \int_{T_{ref}}^T C_{p,k}(T') dT' \right) \quad (9)$$

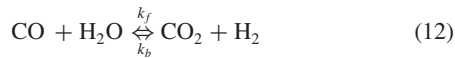
$$\bar{p} = \bar{\rho} R_u \bar{T} \sum_{i=1}^N \frac{\tilde{Y}_i}{W_i} \quad (10)$$

Full account is taken of variable transport and thermodynamic properties. Within the thermodynamic regime of concern in practical rocket-motor environments, the specific heat C_p , viscosity μ , and thermal conductivity λ for individual species are approximated by fourth-order polynomials of temperature. The specific heat of the mixture is obtained by mass fraction weighting of each species. The viscosity of the mixture is obtained through Wilke's method, and the thermal conductivity is calculated by Wassiljewa's approach with the modification of Mason and Saxena, as noted in [13]. The binary mass diffusivity D_{ij} between species i and j is obtained using the Chapman–Enskog theory in conjunction with the Lennard–Jones intermolecular potential energy function [13]. The effective diffusion coefficient D_{im} in a multicomponent mixture can be related to the binary diffusion coefficient D_{ij} through the following equation [14]:

$$D_{im} = (1 - \tilde{X}_i) \left/ \sum_{i \neq j} \frac{\tilde{X}_j}{D_{ij}} \right. \quad (11)$$

B. Gas-Phase Chemical Kinetics

In the current study, the flowfield in the rocket nozzle consists of hot combustion products from the burning of metallized or nonmetallized AP/HTPB composite propellants. The main species in the combustion stream of a nonmetallized propellant are H_2O , CO_2 , CO , HCl , N_2 , and H_2 , along with small amounts of OH and H and negligible concentrations of O_2 and O . In the case of a metallized propellant, a condensed-phase species of Al_2O_3 is also present, in addition to the aforementioned gaseous species. It is assumed that HCl , N_2 , and Al_2O_3 are not involved in the gas-phase chemical reactions. Because the concentrations of O_2 and O are negligible, the oxidation of H_2 and CO to form H_2O and CO_2 , respectively, is also ignored. The most probable reaction occurring in the gas phase is the so-called water–gas shift reaction represented by a one-step global reversible reaction:



Based on the experimental data of Bustamante et al. [15,16], the rates of the forward and reverse reactions take the following forms:

$$\bar{\omega}_{\text{CO}_2} = k_f [\text{CO}]^{0.5} [\text{H}_2\text{O}] \quad (13)$$

$$\bar{\omega}_{\text{CO}} = k_b [\text{H}_2]^{0.5} [\text{CO}_2] \quad (14)$$

The rate constants are expressed in the Arrhenius form as

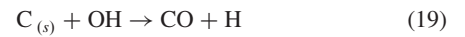
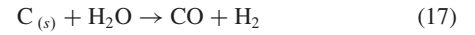
$$k = A \exp(-E_A/R_u T) \quad (15)$$

The chemical kinetics data are obtained by extrapolating the experimental data [15,16] for the temperature and pressure ranges encountered in the current problem. The preexponential factor and the activation energy for the backward rate constant are $5.99 \times 10^8 \text{ (m}^3/\text{kmol}\cdot\text{s}^2)^{0.5}$ and 213.3 kJ/mol , respectively [15]. The corresponding values for the forward rate constant are $2.34 \times 10^{10} \text{ (m}^3/\text{kmol}\cdot\text{s}^2)^{0.5}$ and 288.3 kJ/mol , respectively [16]. Recently, Culbertson et al. [17] conducted experiments to investigate the forward water–gas shift reaction at elevated pressures. In the present analysis, the kinetics data for either k_f or k_b were first chosen, and the other rate constant was estimated from the equilibrium constant K_{eq} . In a manner similar to the approach of Bustamante et al. [15], K_{eq} was estimated with the following temperature-dependent correlation [18]:

$$K_{\text{eq}} = \exp\left(-4.33 + \frac{4577.8}{T}\right) \quad (16)$$

C. Heterogeneous Chemical Reactions at Nozzle Surface

At high temperatures and pressures, the graphite surface is prone to chemical attack by such species as H_2O , CO_2 , OH , H_2 , O_2 , and O , to form primarily CO [2–4,8]. Although the reactivity of graphite with O and O_2 is significant [19,20], this effect can be ignored due to the fuel-rich nature of AP/HTPB propellants, which produce negligible amounts of O and O_2 in the gas phase. There is a disagreement between Tong et al. [21] and other investigators [2,4] concerning the importance of the reaction between $\text{C}_{(s)}$ and H_2 . In the present work, this reaction was excluded based on the kinetics data from Chi and Landahl [22] and the graphite recession studies of Borie et al. [11] and Kuo and Keswani [9]. The assumption is further supported by the experimentally observed decrease in the nozzle recession rate with increasing concentration of H_2 [2,4,6]. Thus, the three heterogeneous chemical reactions considered at the nozzle surface are



The rate of consumption of graphite/carbon–carbon by an oxidizing species i is expressed as

$$\dot{r}_{i,\text{ch}} = k_i p_{i,s}^n \text{ (kg/m}^2 \text{ s)} \quad (20)$$

where

$$p_{i,s} = p_s Y_{i,s} \frac{W_{\text{mix},s}}{W_i} \quad (21)$$

$$k_i = A_i T_s^b \exp(-E_i/R_u T_s) \quad (22)$$

$Y_{i,s}$ and $p_{i,s}$ represent the mass fraction and partial pressure of species i at the surface, respectively; $W_{\text{mix},s}$, p_s , and T_s are the molecular weight of the gas mixture, pressure, and temperature at the surface, respectively; and n is the overall order of the heterogeneous reaction. Based on Eqs. (17–19), the mass rate of consumption of an oxidizing species i at the gas–solid interface is given by

$$\bar{\omega}_i = \dot{r}_{i,\text{ch}} \frac{W_i}{W_C} \quad (23)$$

The reactions of $\text{C}_{(s)}$ with H_2O and CO_2 have been extensively investigated [11,19,23–25]. The kinetics data compiled by Libby and Blake [25] considered the specific rates of both reactions to be equal, with a preexponential factor of $2470 \text{ kg/(m}^2 \cdot \text{atm} \cdot \text{s)}$ and an activation energy of 41.9 kcal/mol . Golovina [24] provided the kinetics data for the reaction between $\text{C}_{(s)}$ and CO_2 with the preexponential factor and activation energy as $158 \text{ kg/(m} \cdot \text{atm} \cdot \text{s)}$ and 40 kcal/mol , respectively. It has been suggested in previous studies [2,7,23] that at high temperatures, H_2O was the most detrimental oxidizing species responsible for nozzle erosion. Consequently, the rate constants for the reactions of $\text{C}_{(s)}$ with H_2O and CO_2 should not be treated identically, as employed by Libby and Blake [25] and Kuo and Keswani [9]. In the current study, the kinetic parameters A_i and E_i are adopted from the experimental data compiled by Bradley et al. [19]. These parameters were used with success by Chelliah et al. [20] and Lee et al. [26] in their studies of carbon ignition and oxidation at high temperatures. Table 1 lists the kinetics data for the three heterogeneous reactions [19,20]. Figure 1 shows a comparison of the reaction rates of $\text{C}_{(s)}$ with H_2O at 1 atm obtained from the kinetics data compiled by Bradley et al. [19] and Libby and Blake [25]. The corresponding orders of reaction are 0.5 and 1.0, respectively. The agreement in the reaction rates at 1 atm appears to be reasonably close. According to Bradley et al. [19], the reaction rates of $\text{C}_{(s)}$ with CO_2 at 1 atm and high temperatures obtained from Golovina [24] are in good agreement with the kinetics

Table 1 Kinetics data^a for heterogeneous surface reactions [19,20]

Surface reaction	A_i	b	E_i , kcal/mol	$\dot{\omega}_i$, kg/m ² /s
$C_{(s)} + H_2O \rightarrow CO + H_2$	$4.8 \times 10^5 \text{ kg}/(\text{m}^2 \cdot \text{s} \cdot \text{atm}^{0.5})$	0.0	68.8	$k_i P_{H_2O}^{0.5}$
$C_{(s)} + CO_2 \rightarrow 2CO$	$9.0 \times 10^3 \text{ kg}/(\text{m}^2 \cdot \text{s} \cdot \text{atm}^{0.5})$	0.0	68.1	$k_i P_{CO_2}^{0.5}$
$C_{(s)} + OH \rightarrow CO + H$	$3.61 \times 10^2 \text{ kg} \cdot \text{K}^{0.5}/(\text{m}^2 \cdot \text{s} \cdot \text{atm})$	-0.5	0.00	$k_i P_{OH}$

^a $k_i = A_i T_s^b \exp(-E_i/R_u T_s)$ and the rate of graphite consumption is obtained in kg/m²/s.

data for the corresponding reaction, as listed in Table 1. The melting and sublimation/pyrolysis of the graphite/carbon-carbon material are not considered because these phenomena [27] are significant only at a surface temperature greater than 4000 K, which is never attained in practical rocket-motor environments.

D. Turbulence Closure

The unclosed terms $\overline{\rho u_i'' u_i''}$, $\overline{\rho E'' u_j''}$, and $\overline{\rho Y_k'' u_j''}$ in Eqs. (2–4), respectively, are treated using a two-layer model that is well calibrated for transpiration and accelerating flows [28,29]. The model shows superior performance in terms of numerical accuracy and convergence, compared with the conventional low-Reynolds-number k - ε schemes. The two-layer model employs the standard k - ε two-equation approach for the bulk flow away from the wall (i.e., the outer layer). The equations representing the transport of turbulent kinetic energy, and its dissipation rates are

$$\frac{\partial \bar{\rho} k}{\partial t} + \frac{\partial (\bar{\rho} \tilde{u}_j k)}{\partial x_j} = \nabla \cdot \left[\left(\mu + \frac{\mu_t}{\sigma_k} \right) \nabla k \right] + \mu_t G - \rho \varepsilon \quad (24)$$

$$\frac{\partial \bar{\rho} \varepsilon}{\partial t} + \frac{\partial (\bar{\rho} \tilde{u}_j \varepsilon)}{\partial x_j} = \nabla \cdot \left[\left(\mu + \frac{\mu_t}{\sigma_\varepsilon} \right) \nabla \varepsilon \right] + C_{\varepsilon 1} \frac{\varepsilon}{k} \mu_t G - C_{\varepsilon 2} \frac{\varepsilon}{k} \rho \varepsilon \quad (25)$$

where

$$G = 2 \left[\left(\frac{\partial \tilde{u}}{\partial x} \right)^2 + \left(\frac{\partial \tilde{v}}{\partial y} \right)^2 + \left(\frac{\partial \tilde{w}}{\partial z} \right)^2 \right] + \left(\frac{\partial \tilde{u}}{\partial y} + \frac{\partial \tilde{v}}{\partial x} \right)^2 + \left(\frac{\partial \tilde{w}}{\partial y} + \frac{\partial \tilde{v}}{\partial z} \right)^2 + \left(\frac{\partial \tilde{u}}{\partial z} + \frac{\partial \tilde{w}}{\partial x} \right)^2 \quad (26)$$

The turbulent eddy viscosity is obtained from the Prandtl-Kolmogorov relation:

$$\mu_t = C_\mu \left(\frac{\rho k^2}{\varepsilon} \right) \quad (27)$$

The standard and well-tested values used for the empirical constants are $\sigma_k = 1.0$, $\sigma_\varepsilon = 1.3$, $C_{\varepsilon 1} = 1.44$, $C_{\varepsilon 2} = 1.92$, and $C_\mu = 0.09$.

Unlike the low-Reynolds-number treatment, which solves the two turbulent transport equations all the way to the surface, the two-layer approach [29] solves only the turbulent kinetic energy equation in the near-surface region (i.e., the inner layer) and greatly reduces the complexities associated with the stiff distributions of turbulent transport properties. The dissipation rate of the turbulent kinetic

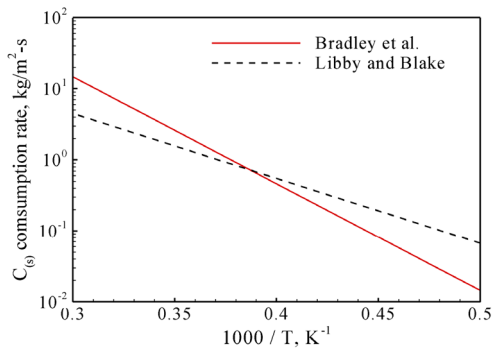


Fig. 1 Comparison of reaction rates [19,25] for $C_{(s)} + H_2O$ at 1 atm.

energy is determined by

$$\varepsilon = \frac{k^{3/2}}{l_\varepsilon} \quad (28)$$

The turbulent eddy viscosity is obtained as

$$\mu_t = C_\mu \rho \sqrt{k} l_\mu \quad (29)$$

The near-wall damping is modeled through specification of the length scales l_μ and l_ε :

$$l_\mu = C_l r_n \left[1 - \exp\left(-\frac{Re_y}{A_\mu} \frac{25}{A^+}\right) \right] \quad (30)$$

$$l_\varepsilon = C_l r_n \left[1 - \exp\left(-\frac{Re_y}{A_\varepsilon}\right) \right] \quad (31)$$

where the turbulent Reynolds number is defined as $Re_y \equiv \sqrt{k} r_n / \nu$, with r_n representing the distance from the surface. The coefficient C_l is given by

$$C_l = \kappa C_\mu^{-3/4} \quad (32)$$

The effect of pressure gradient and surface transpiration is included in A^+ . For an accelerating flow with wall transpiration, it is given by the empirical correlation [30] as

$$A^+ = \frac{24}{7.1 \{v_w^+ + [4.25 P^+ / (1 + 10 v_w^+)]\}} + 1.0 \quad (33)$$

The dimensionless wall blowing velocity v_w^+ and pressure gradient P^+ are given, respectively, by

$$v_w^+ = \frac{u_r}{u_\tau}, \quad P^+ = \frac{\nu}{\rho u_\tau^3} \frac{dp}{dx} \quad (34)$$

where u_r is the velocity at the nozzle surface due to the material erosion and u_τ is the friction velocity. Other constants applied here are $A_\mu = 70.0$ and $A_\varepsilon = 2C_l$. The inner and outer layers are matched at locations where viscous effects are negligible, according to the following criteria. First, the minimum y^+ running along these matching points must be between 80 and 120. Second, the local turbulent Reynolds number Re_y must be larger than 200 in strong turbulent regions. These critical numbers of y^+ and Re_y are taken from the analysis conducted by Chen and Patel [31]. In the present study, the matching of the two layers occurs in the region of $y^+ = 80$ –120 for all the grids employed for various nozzle geometries. After the turbulent eddy viscosity is obtained, the effective viscosity, conductivity, and diffusivity are calculated as follows:

$$\mu_{\text{eff}} = \mu + \mu_t, \quad \lambda_{\text{eff}} = \lambda + \frac{\mu_t C_p}{Pr_t}, \quad D_{\text{eff}} = D + \frac{\mu_t}{\rho Sc_t} \quad (35)$$

A standard value of 0.9 is used for the turbulent Prandtl number Pr_t , and the turbulent Lewis number Le_t is unity.

The turbulence closure scheme was validated against experimental data [32,33] on the skin-friction coefficient and distributions of u^+ and turbulent kinetic energy with y^+ for flows over a flat plate. Furthermore, an extensive numerical study was conducted for various nozzle geometries to benchmark the predicted heat-transfer coefficients. In particular, the nozzle configuration of Back et al.

[34] was considered, and the calculated heat-transfer coefficient compared with the measurements much better than the prediction obtained from the Bartz correlation [35], which is widely used for estimating the convective heat transfer in rocket-nozzle flows.

E. Solid-Phase Governing Equation

With the neglect of thermal decomposition and chemical reactions in the solid phase, the heat conduction in the radial direction is governed by the following equation:

$$\rho_c \frac{\partial h_c}{\partial t} + \frac{\rho_c}{r} \frac{\partial}{\partial r} (r h_c \dot{r}_c) = \frac{1}{r} \frac{\partial}{\partial r} \left(\lambda_c r \frac{\partial T_c}{\partial r} \right) \quad (36)$$

The equation takes into account the effect of surface recession and variable thermophysical properties. Integration of Eq. (36) at steady state across the nozzle material gives

$$r_i \left[\lambda_c \frac{\partial T_c}{\partial r} \right]_{r_i} = \dot{r}_c \rho_c (h_{c-g} r_i - h_o r_o) + r_o \left[\lambda_c \frac{\partial T_c}{\partial r} \right]_{r_o} \quad (37)$$

where r_i and r_o are the inner and outer radii of the nozzle material at any axial location, respectively, and h_{c-g} and h_o are the corresponding specific enthalpies, respectively.

In most existing studies, the outer boundary of the nozzle material is modeled to be adiabatic. Such a treatment is valid when the nozzle material is sufficiently thick or well insulated. The thermal penetration depth ($\sim \alpha_c / \dot{r}_c$) in graphite under a typical nozzle operating condition is on the order of 1 cm, about the thickness of the material. Thus, the enforcement of the adiabatic condition needs to be carefully examined. An adequate sensitivity study on the effect of the outer boundary condition on the nozzle material erosion is required and will be elaborated later.

F. Gas-Solid Interfacial Condition

The processes in the gas and solid phases are matched at the nozzle surface by enforcing the continuities of mass, species, and energy fluxes. The procedure eventually gives the erosion rate of nozzle material. The conservation laws at the gas-solid interface can be written as

Mass:

$$\bar{\rho}_g \tilde{u}_r = \rho_c \dot{r}_c \quad (38)$$

Species:

$$\left(-\bar{\rho}_g D_{km} \frac{d\tilde{Y}_k}{dr} + \bar{\rho}_g \tilde{Y}_k \tilde{u}_r \right) = \bar{\omega}_k \quad (39)$$

Energy:

$$\left[\lambda_c \frac{\partial T_c}{\partial r} \right]_{r_i} + \dot{r}_c \rho_c h_{c-g} = \left[\lambda_g \frac{\partial \tilde{T}_g}{\partial r} \right]_{r_i} + \sum_{k=1}^N \bar{\omega}_k \tilde{h}_{g,k} \quad (40)$$

where \tilde{u}_r stands for the radial velocity in the gas phase due to material erosion. The rate of production of gas-phase species k at the nozzle surface on account of heterogeneous reactions (17–19) is denoted by $\bar{\omega}_k$. The first term in Eq. (40) can be obtained by considering the overall energy balance in the solid phase represented by Eq. (37). Radiation is neglected in Eq. (40) due to the prevalence of convective heat transfer [11,36]. The axial velocity, turbulent kinetic energy, and dissipation rate at the gas-solid interface are

$$u_x = 0, \quad k = 0, \quad \frac{\partial \varepsilon}{\partial r} = 0 \quad (41)$$

Finally, flow symmetry is enforced along the nozzle centerline.

G. Nozzle Recession Rate

The heterogeneous reactions (17–19) consume the oxidizing species H_2O , OH , and CO_2 at the nozzle surface. Concentration

gradients then form in the nozzle flowfield and cause the diffusion of those species toward the surface. At a high surface temperature, the heterogeneous chemical reactions proceed so rapidly that the graphite erosion rate is dictated by the species diffusion process. The diffusion-controlled recession rate $\dot{r}_{i,diff-lim}$ due to an oxidizing species i can be determined by first calculating $\bar{\omega}_{i,diff-lim}$ from Eq. (39) with $\tilde{Y}_i = 0$ and then applying the following equation:

$$\dot{r}_{i,diff-lim} = \bar{\omega}_{i,diff-lim} \frac{W_C}{W_i} \quad (42)$$

At a low surface temperature, the heterogeneous reactions become the rate-controlling process for nozzle erosion due to reduced chemical activity, and the recession rate is obtained purely from the chemical kinetics ($\dot{r}_{i,ch}$).

In [9–12], the species equations were not solved for the mass fractions of the oxidizing species at the surface. The graphite recession rate was calculated empirically as the harmonic mean of the kinetics- and diffusion-limited rates. The former was obtained based on the species concentrations in the core flow. The use of the harmonic mean is not valid for surface reactions, which are not first order. No such assumption is employed in the current model. The graphite recession rate ($\text{kg/m}^2\text{-s}$) due to an oxidizing species i is obtained appropriately as

$$\dot{r}_{i,erosion} = \min(\dot{r}_{i,diff-lim}, \dot{r}_{i,ch}) \quad (43)$$

The contributions of $\dot{r}_{i,ch}$ and $\dot{r}_{i,diff-lim}$ from H_2O , OH , and CO_2 are calculated along the entire nozzle length by means of Eqs. (20) and (42), respectively, for each time step, until the steady-state condition is achieved. The net recession rate (meters per second) of the nozzle surface is determined by

$$\dot{r}_c(x) = \frac{1}{\rho_c} \sum_i \dot{r}_{i,erosion} \quad (44)$$

Mechanical erosion associated with the impingement of alumina particles is not considered even for metallized propellants, because the collision of these particles with the nozzle surface is minimal at the throat and its downstream region.

III. Numerical Treatment

The governing equations and associated boundary conditions are solved numerically by means of a density-based finite volume approach with body-fitted coordinates. A four-stage Runge–Kutta scheme is used for the time integration. The convective fluxes are treated explicitly with a second-order central-difference scheme, following the methodology proposed by Rai and Chakravarthy [37]. The chemical reaction source terms are handled in a semi-implicit manner. To ensure numerical stability and convergence, a fourth-order artificial dissipation based on the scalar dissipation model by Swanson and Turkel [38] is employed. The code was implemented on a parallel computing facility by employing a distributed-memory message passing interconnection, a multiple-instruction/multiple-data model, and structured multiblock domain decomposition. Calculations were conducted on an in-house Beowulf system, with each block on an individual processor. The grid is stretched in the radial direction and clustered near the surface. The centers of the computational cells adjacent to the nozzle surface are located at $y^+ < 1$ to accurately capture the near-wall phenomena. Numerically, $Y_{i,s}$ in Eq. (21) amounts to the species concentration at the center of the first computational cell from the surface. Grid independence studies were carried out for all the nozzle geometries to ensure the independence of the results on the chosen grid.

IV. Nozzle Configurations and Boundary Conditions

Figure 2 shows the baseline nozzle configuration considered here, mimicking the experiments detailed in [39] for the study of the erosion of graphite (G-90) nozzle material. The incoming flow consists of the combustion products of either metallized or

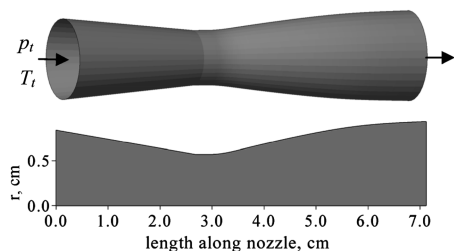


Fig. 2 Baseline nozzle configuration.

nonmetallized AP/HTPB composite propellants. The chamber pressure p_t and temperature T_t are specified at the nozzle inlet. The velocity at the exit is supersonic, and no physical boundary condition needs to be prescribed at that location. Table 2 lists the species mass fractions at the inlet obtained from chemical equilibrium calculations [40] at $p_t = 6.9$ MPa. Six different chamber pressures and their corresponding temperatures are used to study the effect of motor operating conditions on the nozzle-erosion rate. The species mass fractions remain nearly constant in the pressure range of 6.9–45 MPa, except for a noticeable drop in OH at high pressures. Accordingly, OH species was not considered for the chamber pressures above 10 MPa because of its negligible concentration. At a given pressure, the metallized propellant leads to a higher chamber temperature and lower mass fractions of oxidizing species than with its nonmetallized counterpart. Because a single-phase formulation was used, Al_2O_3 was treated as part of the homogeneous mixture. The ambient temperature was taken as 300 K. The thermophysical properties for graphite/carbon–carbon as a function of temperature were adopted from Taylor et al. [41]. Table 3 summarizes the three experimental studies used for validating the current model.

V. Results and Discussions

The theoretical/numerical framework described in the preceding sections was implemented to simulate the chemical erosion of nozzle material in practical rocket-motor environments. The computational domain of the rocket nozzle, shown in Fig. 2, is divided into 141×80 grid points in the x and r directions, respectively. The turbulent flow development in the nozzle is studied first at the steady-state condition. Figure 3 shows the distributions of the temperature, pressure, axial velocity, and Mach number along the centerline for inlet conditions of $T_t = 3000$ K and $p_t = 6.9$ MPa. The nozzle surface is treated as an adiabatic wall without including heterogeneous chemical reactions. The calculations exhibit good agreement with the corresponding one-dimensional results for an isentropic flow with $\gamma = 1.2$. The Mach number increases from 0.28 at the inlet to 2.3 at the exit, but the pressure and temperature decrease monotonically from values slightly less than the chamber conditions to 0.49 MPa and 1890 K, respectively. Figure 4 shows the entire flowfield in terms of temperature, pressure, Mach number, and axial velocity. The flowfield is predominantly one-dimensional except in the thin layer near the surface. The effect of the water–gas shift

reaction [Eq. (12)] in the gas phase is also studied. Figure 5 shows the species-concentration fields including only this reaction, with all other conditions unchanged. The mass fractions of H_2O and CO increase marginally, and those of CO_2 and H_2 decrease accordingly. The gas-phase reactions do not modify the chemical equilibrium significantly. Furthermore, because the water–gas shift reaction is nearly thermally neutral, the temperature field is almost unaffected.

To simulate the erosion of nozzle material, the three heterogeneous reaction [Eqs. (17–19)], along with the energy balance [Eq. (40)], are implemented at the nozzle surface. Figure 6 shows the calculated temperature and species-concentration fields for the case of nonmetallized AP/HTPB propellants. The incoming flow temperature and pressure are $T_t = 3000$ K and $p_t = 6.9$ MPa, respectively, and the outer boundary of the nozzle material is assumed to be adiabatic. As a consequence of surface reactions, the oxidizing species CO_2 , H_2O , and OH are consumed to form CO , H_2 , and H . Concentration gradients then form near the wall. The slight decrease in the N_2 concentration near the surface is attributed to the wall blowing effect associated with the material erosion. Compared with the nonreactive case with an adiabatic wall (Fig. 4), the surface temperature is considerably reduced due to the conductive heat transfer to the nozzle material. The endothermicity of surface reactions also helps lower the surface temperature. The thickness of the species-concentration boundary layer (δ_c) is greater than its velocity counterpart and can be estimated using a simple order-of-magnitude analysis as follows:

$$\delta_c \sim \sqrt{D_{\text{eff}} \tau_f} \quad (45)$$

where D_{eff} is the effective mass diffusivity on the order of 10^{-2} m^2/s . The flow residence time τ_f is approximated as the ratio of the nozzle length to the average axial velocity and has a value of about 0.1 ms. Based on Eq. (45), the concentration boundary-layer thickness thus becomes 1 mm, close to that observed in Fig. 6.

Figure 7 shows the distribution of the erosion rate along the entire length of the nozzle for nonmetallized AP/HTPB with $T_t = 3000$ K and $p_t = 6.9$ MPa. Two points should be noted. First, the erosion rate reaches its maximum (0.124 mm/s) near the throat, mainly due to the enhanced heat transfer in that region. Second, the inclusion of the water–gas shift reaction has a negligible effect on the calculated erosion rate. As such, the remaining computations in the present study were performed by assuming a frozen flow in the gas phase. Although the high temperature prevails in the upstream region of the nozzle throat, the convective heat transfer is relatively small because of low flow velocity. In the downstream region, however, the heat transfer is reduced due to the low-temperature condition resulting

Table 3 Experimental studies of nozzle erosion

Experimental study	Nozzle material	Density, g/cc
Geisler [6]	Bulk graphite	1.83
Borie et al. [11]	Carbon–carbon	1.90
Evans et al. [39]	G-90	1.92

Table 2 Nozzle inlet flow conditions^a

	Nonmetallized AP/HTPB	Metallized AP/HTPB
$Y_{\text{H}_2\text{O}}$	0.29	0.09
Y_{CO_2}	0.22	0.02
Y_{CO}	0.11	0.23
Y_{H_2}	0.003	0.01
Y_{OH}	0.01	0.01
Y_{H}	0.00	0.00
Y_{N_2}	0.10	0.10
$Y_{\text{Al}_2\text{O}_3}$	0.00	0.34
Y_{HCL}	0.267	0.20
p_t , MPa	6.9, 10, 15, 25, 35, 45	6.9, 10, 15, 25, 35, 45
T_t , K	3000, 3020, 3040, 3050, 3060, 3065	3500, 3530, 3550, 3560, 3570, 3575
T_{amb} , K	300	300

^aNozzle material density is 1.92 g/cm³, average nozzle material thickness is 4.8 cm, and throat radius is 0.5715 cm.

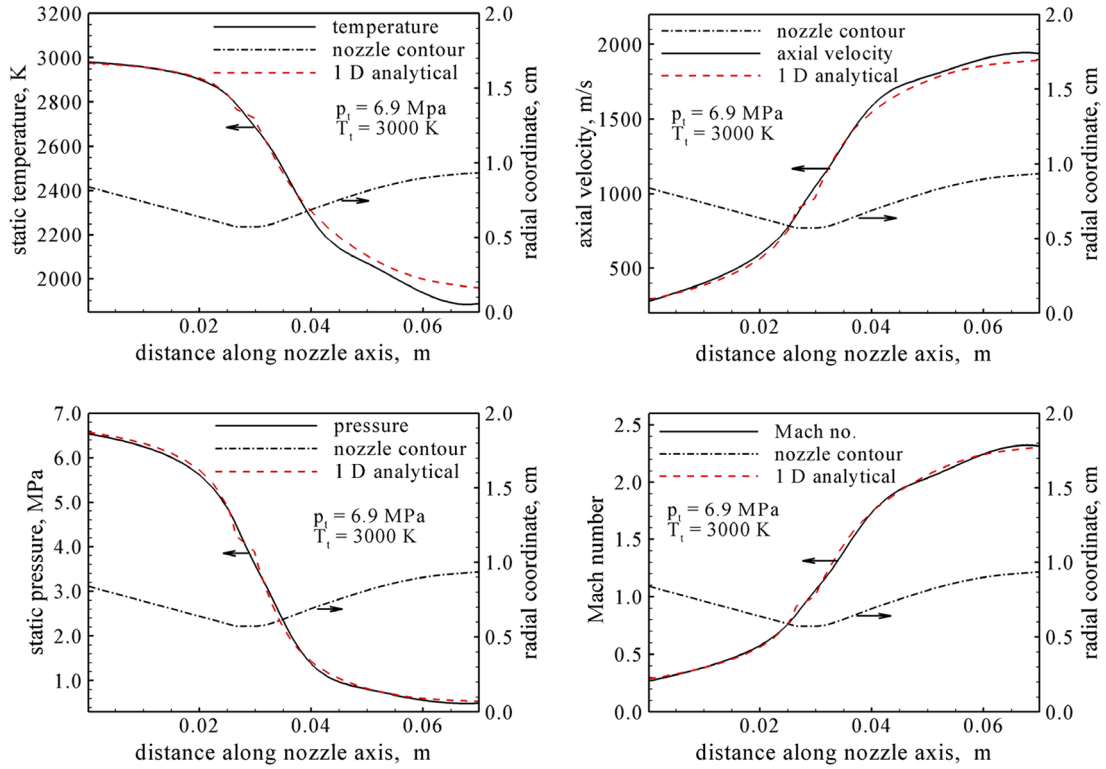


Fig. 3 Distributions of temperature, pressure, axial velocity, and Mach number along the nozzle centerline (nonmetallized propellant, $T_1 = 3000 \text{ K}$, $p_1 = 6.9 \text{ MPa}$, no surface reactions, adiabatic wall).

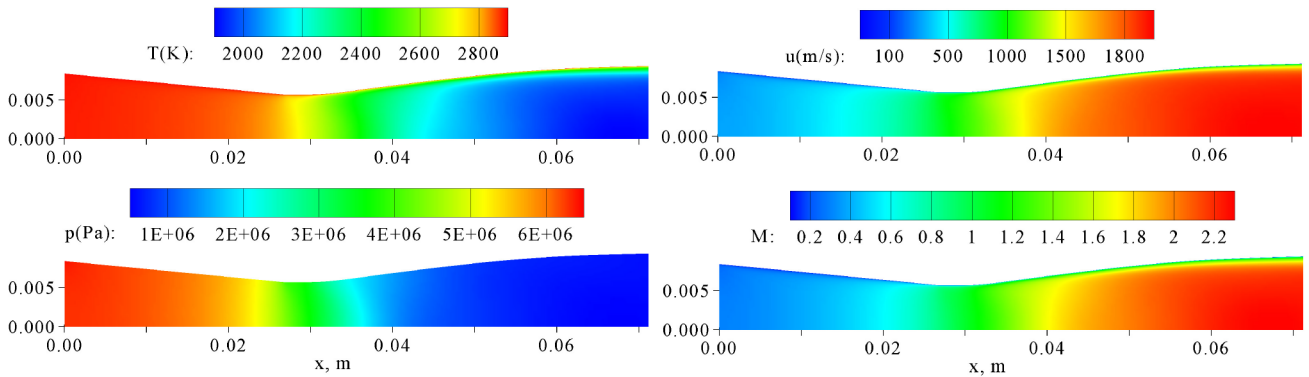


Fig. 4 Distributions of temperature, pressure, axial velocity, and Mach number in the nozzle interior (nonmetallized propellant, $T_1 = 3000 \text{ K}$, $p_1 = 6.9 \text{ MPa}$, no surface reactions, adiabatic wall).

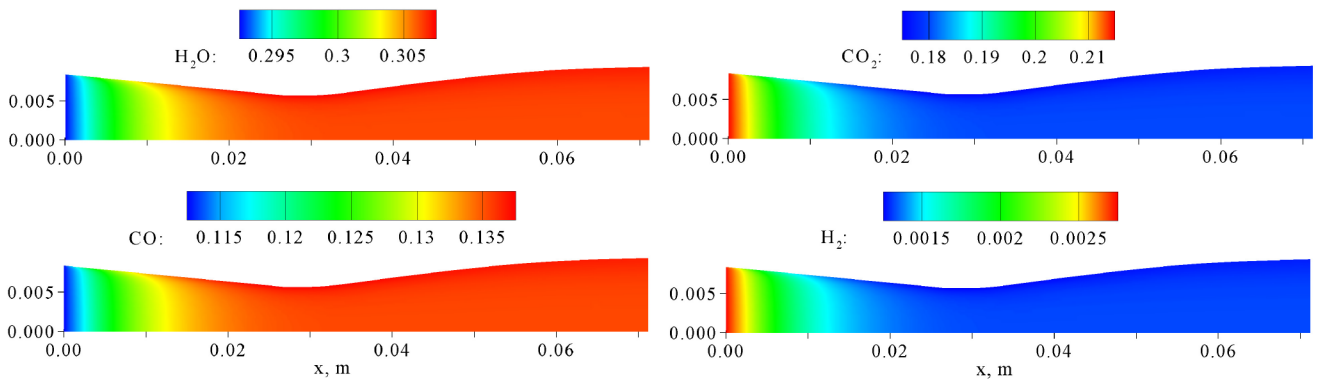


Fig. 5 Distributions of mass fractions of H_2O , CO_2 , CO , and H_2 ; effect of water–gas shift reaction in the gas phase (nonmetallized propellant, $T_1 = 3000 \text{ K}$, $p_1 = 6.9 \text{ MPa}$, no surface reactions, adiabatic wall).

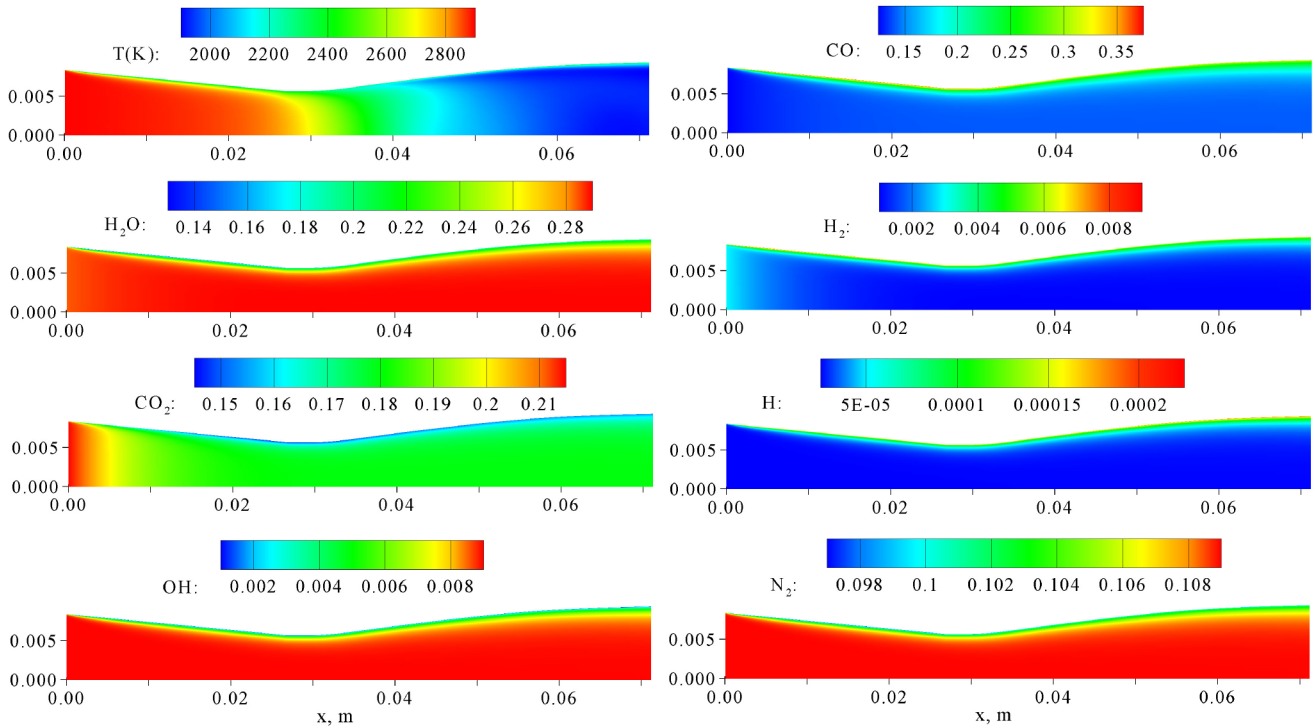


Fig. 6 Distributions of temperature and mass fractions of H_2O , CO_2 , OH , CO , H_2 , H , and N_2 in the nozzle interior (nonmetallized propellant, $T_i = 3000 \text{ K}$, $p_i = 6.9 \text{ MPa}$, with surface reactions, conductive wall).

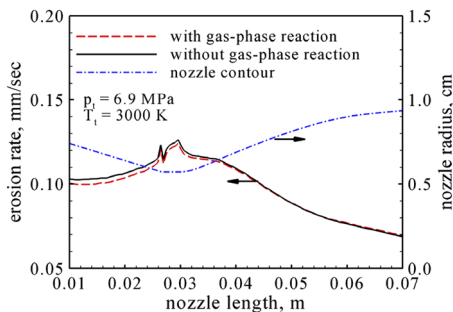


Fig. 7 Nozzle-erosion rate with and without water-gas shift reaction in the gas phase; nonmetallized propellants.

from the flow expansion. In Fig. 7, the small wiggle in the erosion-rate profile arises from the sharp change in the nozzle contour in the throat region. Such small irregularities were not observed in other cases with smooth nozzle profiles.

The dependence of the erosion rate on the outer boundary condition of the nozzle material was also examined, because this condition affects the nozzle surface temperature and associated chemical reaction rates. Table 4 lists three different outer boundary conditions considered herein. The baseline adiabatic condition was relaxed by allowing convective heat transfer at the outer boundary. The heat-transfer coefficient h_{amb} , estimated from standard correlations for turbulent flows over a flat plate, falls in the range of $100\text{--}500 \text{ W/m}^2\text{-K}$, depending on the specific configuration of the nozzle assembly and the vehicle speed. The calculated erosion rate decreases slightly with enhanced heat transfer at the outer boundary. All the results presented subsequently were obtained based on the

adiabatic outer boundary of the nozzle material, following the approach employed by most existing models.

Figure 8 shows the nozzle-erosion rate caused by each of the three oxidizing species H_2O , OH , and CO_2 . Based on the kinetics data employed in the current work (Table 1), the most detrimental species is H_2O , followed by much lesser contributions from OH and CO_2 , in that order. At higher chamber pressures and temperatures, the OH concentration reduces to a very small value and its contribution can be neglected, in comparison with H_2O . Figure 9 shows the distribution of heat flux along the nozzle surface for two different chamber pressures: 6.9 and 10 MPa. As expected, the heat-transfer rate rises with increasing pressure and attains a maximum value in the throat region. The distribution of the erosion rate mimics that of the surface heat flux along the entire nozzle length, indicating a direct correlation between the two quantities.

The radial distributions of the temperature and oxidizing-species concentrations are instrumental in identifying the mechanisms of nozzle material erosion. Figure 10 shows the radial distributions of temperature at the nozzle throat for nonmetallized and metallized propellants. The temperature varies from 2710 K at the centerline to 2285 K at the surface for the former case, and the corresponding temperatures for the latter case are 3170 and 2820 K. Figures 11 and 12 show the radial distributions of the species mass fractions at the nozzle throat for the two propellants. The finite amounts of H_2O and CO_2 and the relatively low temperature ($\sim 2285 \text{ K}$) at the surface for the nonmetallized case indicate that the recession is kinetically controlled for these species. The situation for the metallized propellant is quite different. The concentrations of the three oxidizing species are nearly zero at the nozzle surface because of the relatively high temperature ($\sim 2820 \text{ K}$). Thus, the erosion rate is governed by the diffusion-controlled process. Because the OH mass fraction reduces to zero at the surface for both the propellants, nozzle erosion is diffusion-controlled

Table 4 Effect of outer boundary condition of nozzle material on erosion rates ^a

Outer boundary condition [$\partial T_c / \partial r]_{r_o} = h_{\text{amb}}(T_{c,o} - T_{\text{amb}})$	Erosion rate at throat, mm/s
Adiabatic	0.124
$h_{\text{amb}} = 300 \text{ W/m}^2$, $T_{c,o} = 600 \text{ K}$	0.116
$h_{\text{amb}} = 500 \text{ W/m}^2$, $T_{c,o} = 600 \text{ K}$	0.098

^a $T_{\text{amb}} = 300 \text{ K}$, $T_i = 3000 \text{ K}$, and $p_i = 6.9 \text{ MPa}$; nonmetallized propellant.

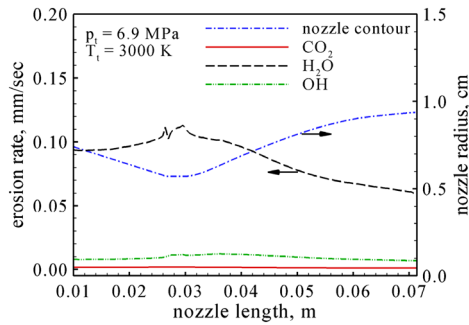


Fig. 8 Nozzle-erosion rate due to various graphite-oxidizing species; nonmetallized propellants.

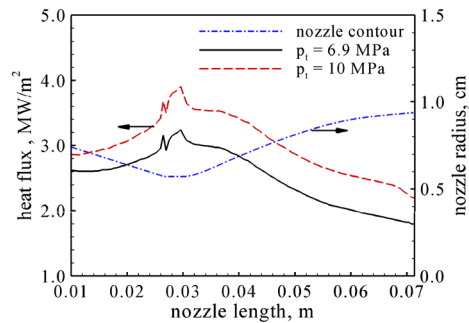


Fig. 9 Distribution of heat flux at the nozzle surface; nonmetallized propellants.

with respect to OH, a phenomenon that can be attributed to the fast reaction between $C_{(s)}$ and OH (Table 1). The transition from the kinetics- to diffusion-controlled mechanism occurs at a surface temperature of around 2800 K. Above this temperature, the reaction rates become sufficiently high to rapidly consume all the oxidizing species diffusing toward the surface. The transition temperature is highly dependent on the chemical kinetics involved and the species concentrations considered at the nozzle inlet and is applicable only to the current problem scenario.

The effect of the chamber pressure on nozzle erosion was studied. Figure 13 shows the erosion-rate profiles for metallized and nonmetallized propellants at a chamber pressure of 25.0 MPa. The corresponding chamber temperatures were 3560 and 3050 K, respectively. The significant difference between the two cases results from different mechanisms that control the recession rate (i.e., chemical kinetics for the nonmetallized case vs species diffusion for the metallized case). Even though the flame temperature of the metallized propellant is much higher than its nonmetallized counterpart, the erosion rate for the former is lower. This can be attributed to the lower concentrations of H_2O and CO_2 (Table 2) in the metallized case due to the formation of alumina, which consumes the majority of the free-molecular oxygen. Figure 14 shows the linear variation of the graphite erosion rate at the nozzle throat with the chamber pressure. Because the convective heat-transfer rate increases with pressure, there is a corresponding rise in the erosion rate. At a chamber pressure greater than ~ 10 MPa, the erosion rate for the nonmetallized case is higher than that for the metallized case. Thus, at high chamber pressures, the erosion rate shows a stronger correlation with the concentrations of the oxidizing species than with the flame temperatures.

The increased densities of the oxidizing species at high pressures also contribute to the severity of the nozzle erosion through their influence on rates of the heterogeneous surface reactions. Figure 15 indicates that the mass fractions of H_2O at the surface of the nozzle throat are 0.134 and 0.099 for two different chamber pressures of 6.9 and 15 MPa, respectively. The high-pressure condition indeed facilitates the reaction of H_2O and graphite, leading to a higher erosion rate. Figures 16 and 17 show the graphite erosion rates along the entire length of the nozzle at various chamber pressures for nonmetallized and metallized AP/HTPB propellants, respectively. The erosion rates attain a maximum value in the throat region in all the cases.

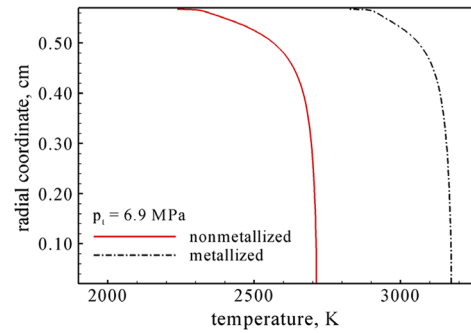


Fig. 10 Radial distributions of temperature at the nozzle throat.

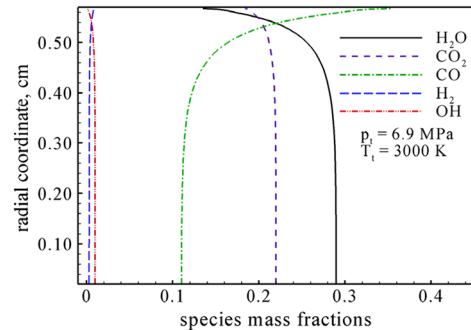


Fig. 11 Radial distributions of species at the nozzle throat; nonmetallized propellant.

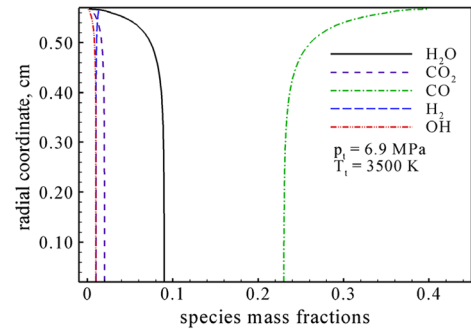


Fig. 12 Radial distribution of species at the nozzle throat; metallized propellant.

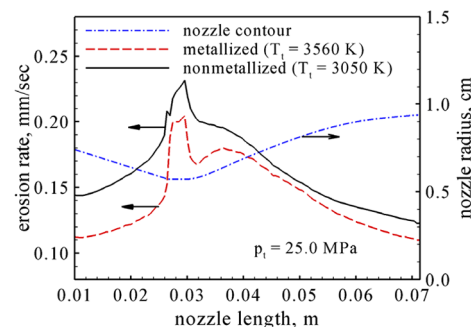


Fig. 13 Nozzle-erosion rates for metallized and nonmetallized propellants at $p_1 = 25$ MPa.

To validate the current analysis, calculations were performed to simulate the nozzle-erosion experiments by Borie et al. [11], Geisler [6], and Evans et al. [39]. Exact nozzle configurations and propellant compositions used in the experiments were treated. Tables 5–7 summarize the nozzle inlet conditions. The oxidizing species OH was not considered because its small concentration resulted in a

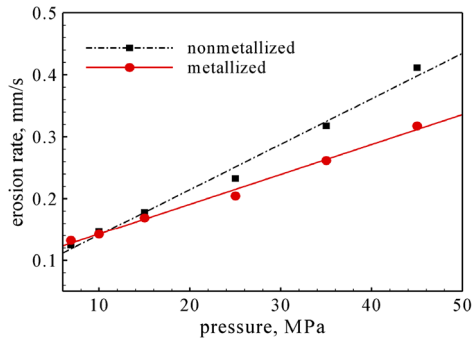


Fig. 14 Effect of chamber pressure on graphite erosion rate at the nozzle throat.

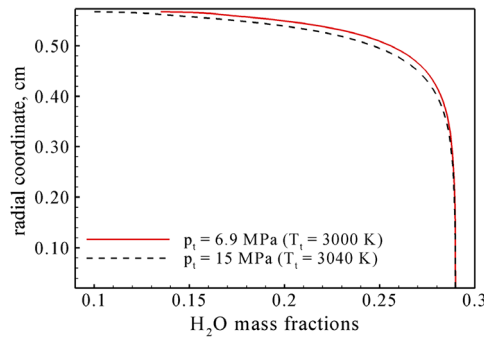


Fig. 15 Radial distribution of H_2O mass fraction at the throat for two different chamber pressures; nonmetallized propellant.

negligible difference in the calculated erosion rates. Borie et al. [11] reported the nozzle recession data obtained by the Société Européenne de Propulsion based on the measured evolution of the nozzle contour during the motor operation and the postfiring analysis. The onset of erosion was detected only after the first 10 s of motor operation. Figure 18 shows the calculated and measured [11] time histories of carbon-carbon nozzle erosion. The calculated erosion rate of 0.130 mm/s at the steady-state condition matches closely with the measured value of 0.139 mm/s.

Geisler [6] employed a BATES (Ballistic Test and Evaluation System) motor to study nozzle material erosion. The instantaneous throat radius was obtained from the measurements of thrust and chamber pressure. Figure 19 shows good agreement between the predictions and measurements [6]. In practice, because it takes about a second to attain the steady-state operating condition, there exists a corresponding time delay in the commencement of the nozzle surface recession. Geisler [6] detected this onset of erosion between 1 and 2 s for all the firings. Accordingly, Fig. 19 includes the time delay at which the erosion was first detected. The model validations given in [9] using the same set of data, however, do not reflect these time delays. Table 8 shows the comparison between the calculated and measured [6] bulk-graphite erosion rates at steady-state conditions. Even though the chamber temperature rises with increasing Al content, the erosion rate decreases. This phenomenon can be attributed to the reduced mass fractions of the oxidizing species H_2O and CO_2 with increasing Al content. Figure 20 shows the radial distribution of the oxidizing species at the nozzle throat for the case with 18% Al. Because the

Table 6 Inlet conditions^a for simulating experiments by Geisler [6]

Y_{CO_2}	Y_{H_2O}	Y_{H_2}	Y_{CO}	Y_{HCL}	$Y_{Al_2O_3}$	Y_{N_2}	p_t , MPa	T_t , K	Al
0.04	0.145	0.02	0.175	0.24	0.28	0.1	6.9	3580	15%
0.025	0.105	0.02	0.18	0.23	0.34	0.1	6.9	3655	18%
0.015	0.07	0.02	0.20	0.195	0.40	0.1	6.9	3715	21%
0.005	0.045	0.02	0.20	0.190	0.44	0.1	6.9	3750	24%
0.0015	0.025	0.02	0.20	0.190	0.47	0.1	6.9	3745	27%

^aNozzle (bulk graphite) density is 1.83 g/cc, average nozzle material thickness is 8 cm, and throat radius is 2.54 cm.

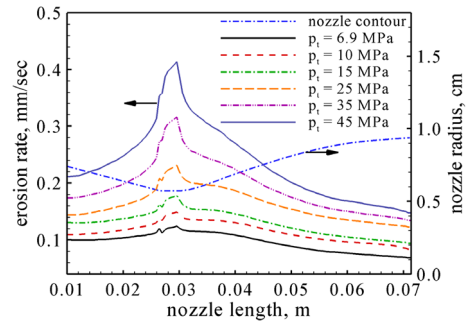


Fig. 16 Graphite erosion rate along the nozzle length at various chamber pressures; nonmetallized propellants.

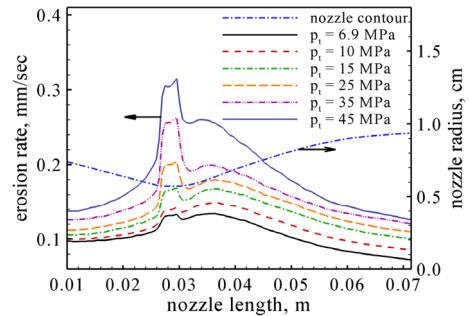


Fig. 17 Graphite erosion rate along the nozzle length at various chamber pressures; metallized propellants.

surface temperature is very high (~ 3000 K), the erosion rate is diffusion-controlled. Consequently, the dependency of the calculated erosion rate on the chemical kinetics data is eliminated. The good agreement between predictions and measurements for metallized propellants corroborates the accuracy of the current model.

In the experimental work by Geisler [6], a significant increase in the nozzle-throat erosion rate was observed when the surface temperature rose above 2600 K. It was postulated that the phenomenon could be attributed to the phase transformation of graphite to a more reactive species called carbyne [42], which exists as a polyne $[-C \equiv C - C \equiv C -]_n$. This phenomenon will be investigated in the future work and is beyond the scope of this paper. For metallized propellants, the graphite-to-carbyne transformation may occur because the surface temperature exceeds 2800 K. But with the current chemical kinetics for graphite, the erosion rate for the metallized case is already diffusion-limited with respect to H_2O , OH, and CO_2 . Even if the reaction rates are higher for carbyne, it is unlikely to have much effect on the erosion rates because the diffusion limit has already been attained. The nozzle erosion,

Table 5 Inlet conditions^a for simulating experiments by Borie et al. [11]

Y_{CO_2}	Y_{H_2O}	Y_{H_2}	Y_{CO}	Y_{HCL}	$Y_{Al_2O_3}$	Y_{N_2}	p_t , MPa	T_t , K
0.035	0.075	0.02	0.20	0.17	0.40	0.1	4.9	3390

^aNozzle (carbon-carbon) density is 1.9 g/cm³, assumed nozzle material thickness is 8–10 cm, and throat radius is 2.54 cm.

Table 7 Inlet conditions^a for simulating experiments by Evans et al. [39]

Case	Y_{CO_2}	$Y_{\text{H}_2\text{O}}$	Y_{H_2}	Y_{CO}	Y_{HCl}	$Y_{\text{Al}_2\text{O}_3}$	Y_{N_2}	Y_{OH}	T_r , K	p_r , MPa
Metallized AP/HTPB	0.02	0.06	0.03	0.25	0.20	0.34	0.1	0.0	3500	8.13
Nonmetallized AP/HTPB	0.21	0.27	0.01	0.11	0.28	0.0	0.11	0.01	3000	8.27

^aNozzle (G-90) density is 1.92 g/cc, average nozzle material thickness is 1.5 cm, and throat radius is 0.508 cm.

however, may increase if carbyne starts reacting with other species such as HCl, CO, or N₂.

The third validation study was based on the experiments of Evans et al. [39] The nozzle surface recession rate was obtained from the pressure and thrust measurements during the motor firings and postfiring analyses. Table 9 lists the calculated and measured graphite erosion rates for the two propellants considered. The agreement is good for the metallized propellant and reasonable for the nonmetallized propellant. In the latter case, the relatively low surface temperature at the throat (~2300 K) renders the material erosion a kinetically controlled process. The discrepancy between the measurement and prediction may arise from the uncertainties in the kinetics data employed for the heterogeneous surface reactions, as well as the uncertainties in experiments. There exists a need to develop a more accurate kinetic mechanism for the specific nozzle material under consideration and for the temperature and pressure ranges in rocket-motor environments.

VI. Conclusions

A comprehensive analysis was established to predict the chemical erosion of graphite/carbon-carbon nozzle materials in solid-propellant rocket motors. Many restrictive assumptions and approximations made in previous models were relaxed. Both nonmetallized and metallized AP/HTPB propellants were considered over a wide range of chamber pressures. Good agreement was achieved with three different sets of experimental data. The key factors dictating the erosion process are motor operating conditions, concentrations of the oxidizing species in the core flow, heterogeneous chemical kinetics at the surface, and nozzle geometry and material properties. The erosion rate is found to be most severe in the throat area,

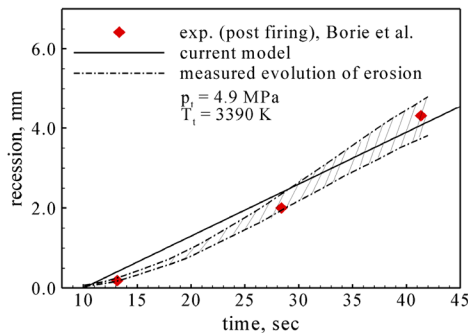


Fig. 18 Comparison between calculated and measured [11] nozzle material (carbon-carbon) erosion.

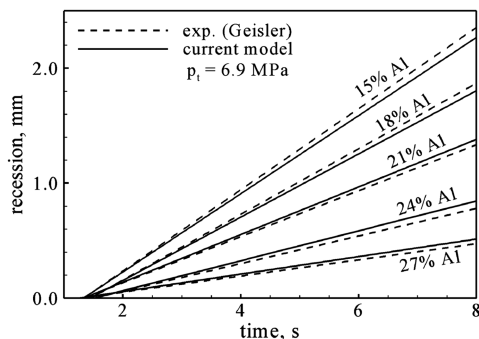


Fig. 19 Comparison between calculated and measured [6] nozzle material (bulk graphite) erosion.

Table 8 Comparison between calculated and measured nozzle recession rates [6]

Al	\dot{r}_{expt} , mm/s	\dot{r}_{model} , mm/s
15%	0.353	0.337
18%	0.284	0.275
21%	0.200	0.207
24%	0.124	0.131
27%	0.069	0.076

due to the maximum heat-transfer rate in that region. H₂O is the most detrimental oxidizing species in dictating the graphite/carbon-carbon nozzle erosion, followed by much lesser contributions from OH and CO₂ in that order. The erosion rate increases linearly with the chamber pressure. At high pressures, the elevated convective heat transfer and enhanced heterogeneous surface reactions contribute to the severity of the material erosion. The chamber temperature is instrumental in determining the nozzle surface temperature, which in turn dictates the rate of heterogeneous surface reactions.

The erosion rate is dictated by heterogeneous chemical kinetics for nonmetallized propellants for which the surface temperatures are low and by a diffusion-controlled process for metallized propellants, for which the surface temperatures are high. The transition from the kinetics- to diffusion-controlled mechanism occurs at a surface temperature of around 2800 K. This transition temperature is highly dependent on the chemical kinetics employed and the species concentrations considered at the nozzle inlet and should be considered specific to the current problem scenario. For the nonmetallized case, the calculated erosion rates are sensitive to the chemical kinetics data employed for the heterogeneous surface reactions. A more accurate kinetic mechanism is needed for the specific nozzle material and propellant formulation under consideration. For metallized propellants, the erosion rate decreases with increasing aluminum content, in spite of the associated increase in the flame temperature. The phenomenon can be attributed to the reduction in mass fractions of the oxidizing species H₂O and CO₂ with increasing aluminum content.

Acknowledgments

This work is supported by the U.S. Office of Naval Research as a part of the Multi-University Research Initiative (MURI) project, funded under contract N00014-04-1-0683, Judah Goldwasser and Cliff Bedford as Contract Monitors. The authors would like to thank Robert Geisler, Kenneth Kuo, and Brian Evans for providing experimental data.

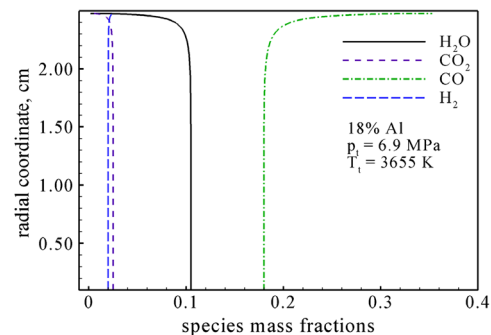


Fig. 20 Radial distribution of species at the nozzle throat for metallized propellant with 18% Al in a BATES motor [6].

Table 9 Comparison between calculated and measured nozzle recession rates [39]

Case	\dot{r}_{expt} , mm/s	\dot{r}_{model} , mm/s
Metallized AP/HTPB	0.084	0.094
Nonmetallized AP/HTPB	0.099	0.125

References

- [1] Sutton, G. P., and Biblarz, O., *Rocket Propulsion Elements*, 7th ed., Wiley-Interscience, New York, 2001.
- [2] Klager, K., "The Interaction of the Efflux of Solid Propellants with Nozzle Materials," *Propellants and Explosives*, Vol. 2, No. 3, 1977, pp. 55–63. doi:10.1002/prop.19770020304
- [3] Delaney, L. J., Eagleton, L. C., and Jones, W. H., "A Semiquantitative Prediction of the Erosion of Graphite Nozzle Inserts," *AIAA Journal*, Vol. 2, No. 8, 1964, pp. 1428–1433.
- [4] McDonald, A. J., and Hedman, P. O., "Erosion of Graphite in Solid-Propellant Combustion Gases and Effects on Heat Transfer," *AIAA Journal*, Vol. 3, No. 7, 1965, pp. 1250–1257.
- [5] McCuen, P. A., Schaefer, J. W., Lundberg, R. E., and Kendall, R. M., "A Study of Solid-Propellant Rocket Motor Exposed Materials Behavior," U.S. Air Force Rocket Propulsion Lab., AFRPL-TR-65-33, Edwards AFB, CA, 1965.
- [6] Geisler, R. L., "The Relationship Between Solid-Propellant Formulation Variables and Nozzle Recession Rates," *JANNAF Rocket Nozzle Technology Subcommittee Meeting*, Lancaster, CA, 12–13 July 1978.
- [7] Swope, L. W., and Berard, M. F., "Effects of Solid-Rocket Propellant Formulations and Exhaust-Gas Chemistries on the Erosion of Graphite Nozzles," *AIAA Solid Propellant Rocket Conference*, Palo Alto, CA, AIAA, Jan. 1964.
- [8] Gowariker, V. R., "Mechanical and Chemical Contributions to the Erosion Rates of Graphite Throats in Rocket Motor Nozzles," *Journal of Spacecraft and Rockets*, Vol. 3, No. 10, 1966, pp. 1490–1494.
- [9] Kuo, K. K., and Keswani, S. T., "A Comprehensive Theoretical Model for Carbon-Carbon Composite Nozzle Recession," *Combustion Science and Technology*, Vol. 42, Nos. 3–4, 1985, pp. 145–164. doi:10.1080/00102208508960374
- [10] Keswani, S. T., and Kuo, K. K., "Validation of an Aerothermochemical Model for Graphite Nozzle Recession and Heat-Transfer Process," *Combustion Science and Technology*, Vol. 47, Nos. 3–4, 1986, pp. 177–192. doi:10.1080/00102208608923872
- [11] Borie, V., Brulard, J., and Lengelle, G., "Aerothermochemical Analysis of Carbon-Carbon Nozzle Regression in Solid-Propellant Rocket Motors," *Journal of Propulsion and Power*, Vol. 5, No. 6, 1989, pp. 665–673.
- [12] Acharya, R., and Kuo, K. K., "Effect of Chamber Pressure and Propellant Composition on Erosion Rate of Graphite Rocket Nozzle," *Journal of Propulsion and Power*, Vol. 23, No. 6, 2007, pp. 1242–1254. doi:10.2514/1.24011
- [13] Reid, R. C., Prausnitz, J. M., and Poling, B. E., *The Properties of Gases and Liquids*, 4th ed., McGraw-Hill, New York, 1987.
- [14] Wilke, C. R., *Chemical Engineering Progress*, Vol. 46, 1950, pp. 95–104.
- [15] Bustamante, F., Enick, R. M., Cugini, A. V., Killmeyer, R. P., Howard, B. H., Rothenberger, K. S., Ciocco, M. V., Morreale, B. D., Chattopadhyay, S., and Shi, S., "High-Temperature Kinetics of the Homogeneous Reverse Water-Gas Shift Reaction," *AIChE Journal*, Vol. 50, No. 5, 2004, pp. 1028–1041. doi:10.1002/aic.10099
- [16] Bustamante, F., Enick, R. M., Killmeyer, R. P., Howard, B. H., Rothenberger, K. S., Cugini, A. V., Morreale, B. D., and Ciocco, M. V., "Uncatalyzed and Wall-Catalyzed Forward Water-Gas Shift Reaction Kinetics," *AIChE Journal*, Vol. 51, No. 5, 2005, pp. 1440–1454. doi:10.1002/aic.10396
- [17] Culbertson, B., Sivaramakrishnan, R., and Brezinsky, K., "Elevated Pressure Thermal Experiments and Modeling Studies on the Water-Gas Shift Reaction," *Journal of Propulsion and Power* (to be published).
- [18] Moe, J. M., "Design of Water-Gas Shift Reactors," *Chemical Engineering Progress*, Vol. 58, No. 3, 1962, pp. 33–36.
- [19] Bradley, D., Dixon-Lewis, G., Habik, El-Din, S., and Mushi, E. M., "The Oxidation of Graphite Powder in Flame Reaction Zones," *20th Symposium (International) on Combustion*, Combustion Inst., Pittsburgh, PA, 1984, pp. 931–940.
- [20] Chelliah, H. K., Makino, A., Kato, I., Araki, N., and Law, C. K., "Modeling of Graphite Oxidation in a Stagnant-Point Flow Field Using Detailed Homogeneous and Semiglobal Heterogeneous Mechanisms with Comparisons to Experiments," *Combustion and Flame*, Vol. 104, No. 4, 1996, pp. 469–480. doi:10.1016/0010-2180(95)00151-4
- [21] Tong, H., Hartman, G. J., Chu, E. K., and Murphy, A. J., "AFRPL Graphite Performance Prediction Program—Improved Capability for the Design and Ablation Performance Prediction of Advanced Air Force Solid Propellant Rocket Nozzles," U.S. Air Force Rocket Propulsion Lab., Rept. AFRPL TR-76-70, Edwards AFB, CA, Dec. 1976.
- [22] Chi, J. W. H., and Landahl, C. E., "Hydrogen Reactions with Graphite Materials at High Temperatures and Pressures," *Nuclear Applications*, Vol. 4, 1968, pp. 159–169.
- [23] Lewis, J. C., Floyd, I. J., and Cowlard, F. C., "A Laboratory Investigation of Carbon-Gas Reactions of Relevance to Rocket Nozzle Erosion," AGARD CP-52, Neuilly sur Seine, France, Feb. 1970.
- [24] Golovina, E. C., "The Gasification of Carbon by Carbon Dioxide at High Temperatures and Pressures," *Carbon*, Vol. 18, No. 3, 1980, pp. 197–201. doi:10.1016/0008-6223(80)90061-5
- [25] Libby, P. A., and Blake, T. R., "Burning Carbon Particles in the Presence of Water Vapor," *Combustion and Flame*, Vol. 41, 1981, pp. 123–147. doi:10.1016/0010-2180(81)90047-X
- [26] Lee, J. C., Yetter, R. A., and Dryer, F. L., "Transient Numerical Modeling of Carbon Particle Ignition and Oxidation," *Combustion and Flame*, Vol. 101, No. 4, 1995, pp. 387–398. doi:10.1016/0010-2180(94)00207-9
- [27] Savvatimskiy, A. I., "Measurements of the Melting Point of Graphite and the Properties of Liquid Carbon (A Review for 1963–2003)," *Carbon*, Vol. 43, No. 6, 2005, pp. 1115–1142. doi:10.1016/j.carbon.2004.12.027
- [28] Rodi, W., "Experience with Two-Layer Models Combining the k - ϵ Model with a One-Equation Model Near the Wall," 29th Aerospace Sciences Meeting, Reno, NV, AIAA Paper 1991-0216, 1991.
- [29] Tseng, I. S., and Yang, V., "Combustion of a Double-Base Homogeneous Propellant in a Rocket Motor," *Combustion and Flame*, Vol. 96, No. 4, 1994, pp. 325–342. doi:10.1016/0010-2180(94)90102-3
- [30] Andersen, P. S., Kays, W. M., and Moffat, R. J., "Experimental Results for the Transpired Turbulent Boundary Layer in an Adverse Pressure Gradient," *Journal of Fluid Mechanics*, Vol. 69, No. 2, 1975, pp. 353–373. doi:10.1017/S00222112075001474
- [31] Chen, H. C., and Patel, V. C., "Near-Wall Turbulence Models for Complex Flows Including Separation," *AIAA Journal*, Vol. 26, No. 6, 1988, pp. 641–648.
- [32] Coles, D. E., and Hirst, E. A., "Computation of Turbulent Boundary Layers," *AFOSS-IFP-Stanford Conference*, Vol. 2, Stanford Univ., Stanford, CA, 1969.
- [33] Wieghardt, K., and Tillman, W., "On the Turbulent Friction Layer for Rising Pressure," NACA TM-1314, 1951.
- [34] Back, L. H., Massier, P. F., and Gier, H. L., "Convective Heat Transfer in a Convergent-Divergent Nozzle," *International Journal of Heat and Mass Transfer*, Vol. 7, No. 5, 1964, pp. 549–568. doi:10.1016/0017-9310(64)90052-3
- [35] Bartz, D. R., "A Simple Equation for Rapid Estimation of Rocket Nozzle Convective Heat Transfer Coefficients," *Jet Propulsion*, Vol. 27, No. 1, 1957, pp. 49–51.
- [36] Keswani, S. T., Andiroglu, E., Campbell, J. D., and Kuo, K. K., "Recession Behavior of Graphite Nozzles in Simulated Rocket Motors," *Journal of Spacecraft and Rockets*, Vol. 22, No. 4, 1985, pp. 396–397.
- [37] Rai, M. M., and Chakravarthy, S., "Conservative High-Order Accurate Finite Difference Method for Curvilinear Grids," AIAA Paper 93-3380, 1993.
- [38] Swanson, R. C., and Turkel, E., "On Central-Difference and Upwind Schemes," *Journal of Computational Physics*, Vol. 101, No. 2, 1992, pp. 292–306. doi:10.1016/0021-9991(92)90007-L
- [39] Evans, B., Kuo, K. K., Ferrara, P. J., Moore, J. D., Kutzler, P., and Boyd, E., "Nozzle Throat Erosion Characterization Study Using a Solid-Propellant Rocket Motor Simulator," 43rd AIAA/ASME/SAE/ASEE Joint Propulsion Conference and Exhibit, AIAA Paper 2007-5776, July 2007.
- [40] Gordon, S., and McBride, B. J., "Computer Program for Calculation of Complex Chemical Equilibrium Compositions and Applications," NASA, Ref. Publ. 1311, 1994.
- [41] Taylor, R. E., Groot, H., and Shoemaker, R. L., "Thermophysical Properties of Fine Weave Carbon/Carbon Composites," 16th AIAA Thermophysics Conference, AIAA Paper 1981-1103, 1981.
- [42] Whittaker, A. G., "Carbon: A New View of Its High-Temperature Behavior," *Science*, Vol. 200, No. 4343, 1978, pp. 763–764. doi:10.1126/science.200.4343.763